Editors' Suggestion

Fractional Chern insulator states in multilayer graphene moiré superlattices

Zhongqing Guo [1,*], Xin Lu [1,*], Bo Xie [1], and Jianpeng Liu [1,2,3,†]

[1]*School of Physical Science and Technology, ShanghaiTech University, Shanghai 201210, China*

[2]*ShanghaiTech Laboratory for Topological Physics, ShanghaiTech University, Shanghai 201210, China*

[3]*Liaoning Academy of Materials, Shenyang 110167, China*

(Received 21 December 2023; revised 1 July 2024; accepted 18 July 2024; published 6 August 2024)

In this work, we theoretically study the fractional Chern insulator (FCI) states in rhombohedral multilayer graphene moiré superlattices. We start from the highest energy scale (∼2 eV) of the continuum model, and construct a renormalized low-energy model that applies to a lower cutoff ∼0.15 eV using a renormalization group approach. Then, we study the ground states of the renormalized low-energy model at filling 1 under the Hartree-Fock approximation in the presence of tunable but self-consistently screened displacement field D with several experimentally relevant background dielectric constants ϵ_r. Focusing on the pentalayer moiré graphene system, two competing Hartree-Fock states are obtained at filling 1, which give rise to two types of topologically distinct isolated flat bands with Chern numbers 1 and 0, respectively. By hole-doping the isolated topological flat bands, both Laughlin-type and composite-fermion-type FCI states can be obtained through exact-diagonalization calculations at different fractional filling factors, which exhibit quantitative consistency with experimental measurements. We further explore the correlated topological states in generic rhombohedral multilayer graphene moiré superlattices, and find that FCI states may also emerge in tetralayer and hexalayer moiré graphene systems.

DOI: 10.1103/PhysRevB.110.075109

I. INTRODUCTION

Recent experimental discoveries of fractional quantum anomalous Hall effects in both twisted transition metal dichalcogenides (TMDs) [1–4] and graphene moiré superlattices [5] have led to significant research interest in the condensed matter community. The fractional quantum anomalous Hall state is also known as the fractional Chern insulator (FCI) state [6–12], which is the zero-field analog of the fractional quantum Hall effect [13–18]. Different types of FCI states have been theoretically studied in various lattice models [19–24].

In order to realize the FCI state, an isolated topological flat band with nonzero Chern number and desirable quantum geometric properties is required [25–30]. The two-dimensional moiré superlattice provides an ideal platform to achieve such topological flat bands with tunable valley Chern numbers. For example, in "magic-angle" twisted bilayer graphene (TBG), the lowest two bands (per spin per valley) become ultraflat [31], and are found to be topologically nontrivial with Landau-level-like wave functions [32–41]. Such topological flat bands are also proposed to exist in moiré superlattices consisting of nearly aligned hexagonal boron nitride (hBN) and rhombohedral graphene multilayers [42–46], twisted multilayer graphene [47–56], and moiré TMD [57–66] systems. By virtue of the interplay between nontrivial topology and strong e-e interaction effects in such topological flat bands, integer quantum anomalous Hall effects [67–69] and field-driven Chern insulators [70–74] have been realized. Nevertheless, characteristics of FCI states from compressibility measurements and optical measurements are observed only in a few systems [75,76], including heterostructures of bilayer graphene and hBN [75] and magic-angle TBG [76] under magnetic fields, and twisted TMDs [3,4]. Direct transport evidence of FCIs with fractionally quantized Hall conductivities under zero magnetic field has been observed recently in twisted TMDs and aligned hBN–pentalayer graphene (PLG) moiré superlattices [1,2,5].

In particular, several integer and fractionally quantized plateaus of anomalous Hall resistances have been observed in a moiré superlattice consisting of aligned hBN and rhombohedral stacking of PLG at integer and fractional filling factors [5], which calls for microscopic understandings. In this work, combining renormalization group (RG), Hartree-Fock (HF), and exact-diagonalization (ED) methods developed based on the continuum model of hBN-aligned multilayer graphene moiré superlattices, we study the interacting ground states of the systems at both integer and fractional filling factors. Including effects of remote-band renormalization and self-consistent screening of D fields, within the unrestricted Hartree-Fock framework, we obtain a spin-valley polarized integer Chern-insulator state with Chern number 1 at filling 1 for $D \lessapprox 1$ V/nm for the PLG system, which competes with another trivial, Chern-number-zero Hartree-Fock state. The two HF states would give rise to two types of isolated flat bands right below the chemical potential (of filling 1) with distinct topological characters. Then, we consider hole-doping both types of topologically distinct HF flat bands, and study the interacting ground states at hole dopings of 1/3, 2/5, 3/5, and 2/3 (corresponding to electron fillings

*These authors contributed equally to this work.

†Contact author: liujp@shanghaitech.edu.cn

of 2/3, 3/5, 2/5, and 1/3 with respect to charge neutrality) in the presence of self-consistently screened D fields. Both Laughlin-type (at 2/3 filling) and composite-fermion-type (at 3/5 filling) FCI states are obtained, which exhibit quantitative consistency with experimental measurements [5]. We further explore the correlated and topological states in generic multilayer graphene moiré systems, and find that FCI states may also emerge in tetralayer and hexalayer moiré graphene systems at 2/3 filling.

The remaining part of the paper is organized as follows. In Sec. II, we first introduce the continuum model of multilayer graphene–hBN moiré superlattices and describe the method to take into account electrostatic screening of the external displacement field. In Sec. III, we discuss how the low-energy single-particle properties would be renormalized by Coulomb interactions with remote-band electrons, and present renormalization group equations. In Sec. IV, we present the Hartree-Fock phase diagram at filling factor 1 of the moiré bands, with a discussion on the integer quantum anomalous Hall state and the properties of the isolated topological flat band emerging from such a state. In Sec. V, we first discuss the workflow of the ED calculations, then present the phase diagram of many-body ground states in pentalayer graphene–hBN moiré superlattices at 1/3, 2/3, 2/5, and 3/5 fillings obtained from ED calculations. Finally, in Sec. VI, we present the phase diagrams of FCI states in generic rhombohedral multilayer graphene moiré superlattices, and conclude the paper in Sec. VII.

II. CONTINUUM MODEL

In our theoretical study, we adopt the continuum model derived by Moon and Koshino [78] to multilayer graphene–hBN moiré superlattices. Taking PLG as an example, the effective Hamiltonian of the system around the K or K' valleys can be properly described by the following noninteracting continuum model,

$$H^{0,\mu} = H^{0,\mu}_{\text{penta}} + V_{\text{hBN}}, \tag{1}$$

where $H^{0,\mu}_{\text{penta}}$ is the noninteracting $\mathbf{k}\cdot\mathbf{p}$ Hamiltonian of rhombohedral PLG of valley μ ($\mu = \pm$ standing for K/K' valley), and V_{hBN} denotes the moiré potential exerted on the bottom graphene layer closest to the aligned hBN substrate. More specifically, $H^{0,\mu}_{\text{penta}}$ is composed of the intralayer term $h^{0,\mu}_{\text{intra}}$ and the interlayer term $h^{0,\mu}_{\text{inter}}$:

$$H^{0,\mu}_{\text{penta}} = \begin{pmatrix} h^{0,\mu}_{\text{intra}} & \left(h^{0,\mu}_{\text{inter}}\right)^\dagger & 0 & 0 & 0 \\ h^{0,\mu}_{\text{inter}} & h^{0,\mu}_{\text{intra}} & \left(h^{0,\mu}_{\text{inter}}\right)^\dagger & 0 & 0 \\ 0 & h^{0,\mu}_{\text{inter}} & h^{0,\mu}_{\text{intra}} & \left(h^{0,\mu}_{\text{inter}}\right)^\dagger & 0 \\ 0 & 0 & h^{0,\mu}_{\text{inter}} & h^{0,\mu}_{\text{intra}} & \left(h^{0,\mu}_{\text{inter}}\right)^\dagger \\ 0 & 0 & 0 & h^{0,\mu}_{\text{inter}} & h^{0,\mu}_{\text{intra}} \end{pmatrix}. \tag{2}$$

Here, the intralayer part is just the monolayer $\mathbf{k}\cdot\mathbf{p}$ model

$$h^{0,\mu}_{\text{intra}} = -\hbar v^0_F\, \mathbf{k}\cdot\boldsymbol{\sigma}_\mu, \tag{3}$$

where $\hbar v^0_F \approx 5.253$ eV Å is the noninteracting Fermi velocity of Dirac fermions in monolayer graphene derived from the Slater-Koster tight-binding model [77,79], $\mathbf{k}$ is the wave vector expanded around the Dirac point from valley μ, and $\boldsymbol{\sigma}_\mu = (\mu\sigma_x, \sigma_y)$ is the Pauli matrix defined in sublattice space. The interlayer term is expressed as

$$h^{0,\mu}_{\text{inter}} = \begin{pmatrix} \hbar v_\perp(\mu k_x + i k_y) & t_\perp \\ \hbar v_\perp(\mu k_x - i k_y) & \hbar v_\perp(\mu k_x + i k_y) \end{pmatrix}, \tag{4}$$

where $t_\perp = 0.34$ eV, $\hbar v_\perp = 0.335$ eV Å are extracted from the Slater-Koster hopping parameters [77,79]. The moiré potential reads [78]

$$V_{\text{hBN}}(\mathbf{r}) = V^{\text{eff}}(\mathbf{r}) + M^{\text{eff}}(\mathbf{r})\sigma_z + e v_F \mathbf{A}^{\text{eff}}(\mathbf{r})\cdot\boldsymbol{\sigma}_\mu, \tag{5}$$

where we classify different terms in the effective potential by their sublattice structure. Simple algebra calculations give

$$V^{\text{eff}}(\mathbf{r}) = V_0 - V_1 \sum_{j=1}^{3} \cos\alpha_j(\mathbf{r}), \tag{6a}$$

$$M^{\text{eff}}(\mathbf{r}) = \sqrt{3} V_1 \sum_{j=1}^{3} \sin\alpha_j(\mathbf{r}), \tag{6b}$$

$$e v_F \mathbf{A}^{\text{eff}}(\mathbf{r}) = 2\mu V_1 \sum_{j=1}^{3} \begin{pmatrix} \cos[2\pi(j+1)/3] \\ \sin[2\pi(j+1)/3] \end{pmatrix} \cos\alpha_j(\mathbf{r}), \tag{6c}$$

$$\alpha_j(\mathbf{r}) = \mathbf{G}_j\cdot\mathbf{r} + \psi + \frac{2\pi}{3} \quad \text{with} \quad \mathbf{G}_3 = -\mathbf{G}_1 - \mathbf{G}_2, \tag{6d}$$

where $V_0 = 0.0289$ eV, $V_1 = 0.0210$ eV, and $\psi = -0.29$ rad.

To simulate large D ($D \sim 1$ V/nm) in the experiments, we need to take into account the electrostatic screening effect to find the actual on-site energy differences between layers in pentalayer graphene at various background dielectric constants ϵ_r. To encounter the screening effect, we start enforcing a fixed external electric field $E_{\text{ext}} = D/\epsilon_{\text{hBN}}$ to pentalayer graphene with the dielectric constant of hBN $\epsilon_{\text{hBN}} = 4$. This would induce a constant electrostatic potential difference between the two adjacent layers $eE_{\text{ext}}d_0$ ($e > 0$), which is added to the diagonal part in the Hamiltonian of pentalayer graphene Eq. (2). Then, we solve the Hamiltonian and retrieve the distribution of excess electrons in each layer. The unevenly distributed electrons would induce an additional electric field to counteract E_{ext} so as to cancel out part of the electrostatic potential difference between layers. This screening process is treated by solving the classical Poisson equation in electrostatics with a background dielectric constant ϵ_r, while the charge density is calculated quantum mechanically using the continuum model described above. More details can be found in Ref. [78] and in Secs. I and II of the Supplemental Material [77].

We first focus on the PLG system in which fractional quantum anomalous Hall effects have been experimentally realized [5]. Specifically, we consider a moiré superlattice consisting of rhombohedral stacking of PLG encapsulated by hBN substrates on both sides. Only on the bottom side, hBN is nearly aligned with PLG with a twist angle of 0.77° (consistent with

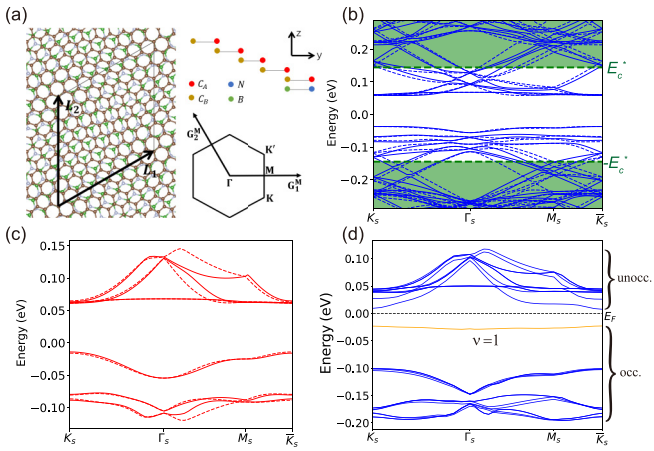

FIG. 1. (a) Schematic illustration of PLG-hBN moiré superlattice with boron (nitrogen) aligned with B (A) sublattice in the AA region. Results with other hBN alignments can be found in the Supplemental Material [77]. (b)–(d) show continuum model band structures with twist angle 0.77°, $D = 0.97$ V/nm, and $\epsilon_r = 5$. (b) The bare noninteracting band structures, where the green dashed lines mark the low-energy window E_C^*, and the green area denotes the remote bands. (c) Low-energy band structures within E_C^* with renormalized continuum model parameters given by Eq. (14). The solid and dashed lines in (b) and (c) represent the bands from K and K' valleys, respectively. (d) Hartree-Fock band structures at filling $\nu = 1$, where the gray dashed line marks the chemical potential. The orange line marks the isolated flat band.

the experimental setup in Ref. [5]), leading to a commensurate moiré superlattice with lattice constant $L_s = 109$ Å, as schematically shown in Fig. 1(a). The corresponding moiré Brillouin zone is presented in Fig. 1(a). A vertical displacement field would induce an electrostatic potential drop across PLG, which would induce the redistribution of charge density among different layers. This in turn screens the external displacement field, which is treated self-consistently [77,80] assuming a background dielectric constant ϵ_r ($4 \leqslant \epsilon_r \leqslant 8$). This background dielectric constant encompasses all other screening effects, including the polarizability of carbon orbitals [81], electron-hole fluctuations, substrate effects, etc. For the sake of consistency, the same dielectric constant ϵ_r has been used in the following RG, HF, and ED calculations.

In Fig. 1(b) we show the noninteracting band structures of PLG-hBN moiré superlattices with twist angle 0.77° under (self-consistently screened) displacement field $D = 0.97$ V/nm. Clearly the valence moiré bands are energetically separated from the conduction ones by a sizable gap ~95 meV, while the conduction moiré bands are all entangled, which disfavors the FCI state at electron doping at this moment.

III. RENORMALIZED BAND STRUCTURES

Although we focus on the low-energy physics within $E_C^* \sim 0.15$ eV, the presence of filled high-energy valence bands indeed plays an important role considering e-e interactions. The electrons in the filled remote bands outside E_C^* will act through long-ranged Coulomb potential upon the dynamics of low-energy electrons such that an effective low-energy Hamiltonian (within E_C^*) would have parameters in general larger in amplitudes than the noninteracting ones. We take into account this effect using the perturbative renormalization group (RG) approach.

Specifically, outside E_C^*, the continuum model is approximately particle-hole symmetric, which allows for a particle-hole symmetric form of the Coulomb interaction [82]:

$$\hat{V}_{\rm int}(E_c) = \frac{1}{2}\int d^2\mathbf{r}d^2\mathbf{r}' V_c(\mathbf{r}-\mathbf{r}')[\hat{\rho}(\mathbf{r}) - \bar{\rho}_{E_c}(\mathbf{r})] \times [\hat{\rho}(\mathbf{r}') - \bar{\rho}_{E_c}(\mathbf{r}')], \tag{7}$$

with

$$\bar{\rho}_{E_c}(\mathbf{r}) = \frac{1}{2}\sum_{\substack{\sigma,n,\mathbf{k};\\ |\epsilon_{n,\mathbf{k}}|\leqslant E_c}} \phi^*_{\sigma n\mathbf{k}}(\mathbf{r})\phi_{\sigma n\mathbf{k}}(\mathbf{r}), \tag{8}$$

where E_C is the overall energy cutoff of the continuum model, i.e., the largest energy scale in the problem. Here $\phi_{\sigma n\mathbf{k}}(\mathbf{r})$ is the wave function of an eigenstate of the noninteracting continuum model Hamiltonian with energy $\epsilon_{n,\mathbf{k}}$, with σ, n, $\mathbf{k}$ referring to the spin, band index, and wave vector, respectively. Note that for simplicity, here the valley index has been included in the band index n.

Now we change the cutoff E_c to a smaller one E_c' and see how these parameters are modified by $\hat{V}_{\rm int}$, which can be treated perturbatively when E_c' is much larger than any other energy scale in the system. To do so, we split the field operator $\hat{\psi}(\mathbf{r}) = \hat{\psi}^<(\mathbf{r}) + \hat{\psi}^>(\mathbf{r})$, where

$$\hat{\psi}^<(\mathbf{r}) = \sum_{\substack{\sigma,n,\mathbf{k};\\ |\epsilon_{n,\mathbf{k}}|\leqslant E_c'}} \phi_{\sigma n\mathbf{k}}(\mathbf{r})\hat{c}_{\sigma n}(\mathbf{k}), \tag{9}$$

$$\hat{\psi}^>(\mathbf{r}) = \sum_{\substack{\sigma,n,\mathbf{k};\\ E_c'<|\epsilon_{n,\mathbf{k}}|\leqslant E_c}} \phi_{\sigma n\mathbf{k}}(\mathbf{r})\hat{c}_{\sigma n}(\mathbf{k}). \tag{10}$$

Then, we integrate out the fast modes $\hat{\psi}^>(\mathbf{r})$ in $\hat{V}_{\rm int}(E_c)$, and the e-e interaction in the lower energy window delimited by E_c' is

$$\hat{V}_{\rm int}(E_c') = \frac{1}{2}\int d^2\mathbf{r}d^2\mathbf{r}' V_c(\mathbf{r}-\mathbf{r}')[\hat{\rho}^<(\mathbf{r}) - \bar{\rho}_{E_c'}(\mathbf{r})] \times [\hat{\rho}^<(\mathbf{r}') - \bar{\rho}_{E_c'}(\mathbf{r})] + \frac{1}{2}\int d^2\mathbf{r}d^2\mathbf{r}' V_c(\mathbf{r}-\mathbf{r}')\hat{\psi}^{<\dagger}(\mathbf{r})\mathcal{F}(\mathbf{r},\mathbf{r}')\hat{\psi}^<(\mathbf{r}') \tag{11}$$

with

$$\mathcal{F}(\mathbf{r},\mathbf{r}') = \sum_{\substack{\sigma,n,\mathbf{k};\\ E_c'<|\epsilon_{n,\mathbf{k}}|\leqslant E_c}} \mathrm{sgn}(\epsilon_{n,\mathbf{k}})\phi_{\sigma n\mathbf{k}}(\mathbf{r})\phi^*_{\sigma n\mathbf{k}}(\mathbf{r}'), \tag{12}$$

which can be calculated using the single-particle Green's function. After some sophisticated calculations, one obtains the following RG flow equations:

$$\frac{dv_F}{d\ln E_c} = -\frac{e^2}{16\pi\epsilon_0\epsilon_r}, \tag{13a}$$

$$\frac{d(ev_F\mathbf{A}^{\rm eff})}{d\ln E_c} = -\frac{e^2}{16\pi\epsilon_0\epsilon_r v_F}, \tag{13b}$$

$$\frac{dt_\perp}{d\ln E_c} = -\frac{e^2}{16\pi\epsilon_0\epsilon_r v_F}, \tag{13c}$$

$$\frac{dM^{\rm eff}}{d\ln E_c} = -2\times\frac{e^2}{16\pi\epsilon_0\epsilon_r v_F}, \tag{13d}$$

$$\frac{dV^{\rm eff}}{d\ln E_c} = 0, \tag{13e}$$

$$\frac{dv_\perp}{d\ln E_c} = 0. \tag{13f}$$

Equation (14) follow after taking integration over E_C, with the low-energy cutoff to be $E_C^* \sim 0.15$ eV, which approximately includes 3 valence bands and 3 conduction bands per spin per valley.

The noninteracting continuum model discussed above applies to an energy cutoff $E_C \sim 2$ eV. Long-range *e-e* interaction effects within this energy window have been neglected. However, it is well known that *e-e* Coulomb interactions would significantly renormalize the effective parameters of the noninteracting model, as in the case of monolayer graphene [83–86] and magic-angle TBG [82]. To this end, we set up a low-energy window $|E| < E_C^* \sim n_{\rm cut}\hbar v_F^0/L_s$ ($E_C^* \sim 150$ meV for $n_{\rm cut} = 3$) as marked by the green dashed lines in Fig. 1(b). Here $2n_{\rm cut}$ may be interpreted as the number of moiré bands (per spin per valley) within the low-energy window E_C^*. Outside the low-energy window marked by E_C^*, the effects of long-range Coulomb interactions are treated by the perturbative RG approach [82,87], which yields a set of renormalized continuum model parameters [77]

$$v_F(E_C^*) = v_F^0\left(1+\frac{\alpha_0}{4\epsilon_r}\ln\frac{E_C}{E_C^*}\right), \tag{14a}$$

$$ev_F\mathbf{A}_{\rm eff}(E_C^*) = ev_F\mathbf{A}_{\rm eff}\left(1+\frac{\alpha_0}{4\epsilon_r}\ln\frac{E_C}{E_C^*}\right), \tag{14b}$$

$$t_\perp(E_C^*) = t_\perp\left(1+\frac{\alpha_0}{4\epsilon_r}\ln\frac{E_C}{E_C^*}\right), \tag{14c}$$

$$M_{\rm eff}(E_C^*) = M_{\rm eff}\left(1+\frac{\alpha_0}{4\epsilon_r}\ln\frac{E_C}{E_C^*}\right)^2, \tag{14d}$$

$$V_{\rm eff}(E_C^*) = V_{\rm eff}, \tag{14e}$$

$$v_\perp(E_C^*) = v_\perp. \tag{14f}$$

In Fig. 1(c) we present the *renormalized* band structures within the $n_{\rm cut} = 3$ low-energy window, with RG-corrected continuum model parameters given by Eq. (14). We see that the lowest conduction moiré band is pushed down in energy and becomes less entangled with other bands due to the renormalization effects from the remote bands. More details of the RG calculations can be found in Sec. III of the Supplemental Material [77].

IV. HARTREE-FOCK PHASE DIAGRAM

We continue to discuss the *e-e* interaction effects within the $n_{\rm cut} = 3$ low-energy window with the renormalized continuum model. Here we consider the dominant intravalley long-range Coulomb interactions,

$$H^{\rm int} = \frac{1}{2N_s}\sum_{\lambda\lambda',\alpha\alpha',ll'} \times \sum_{\mathbf{k}\mathbf{k}'\mathbf{q}} V_{ll'}(\mathbf{q})\,\hat{c}^\dagger_{\mathbf{k}+\mathbf{q},\lambda l\alpha}\,\hat{c}^\dagger_{\mathbf{k}'-\mathbf{q},\lambda' l'\alpha'}\,\hat{c}_{\mathbf{k}'l'\alpha'}\,\hat{c}_{\mathbf{k},\lambda l\alpha}, \tag{15}$$

where N_s denotes the total number of moiré primitive cells in the system, $\mathbf{k}$, $\mathbf{k}'$, and $\mathbf{q}$ represent wave vectors relative to the Dirac points, $\lambda \equiv (\mu,\sigma)$ is a composite index denoting valley μ and spin σ, while l and α are layer and sublattice indices. Since the PLG has a thickness of 1.34 nm, four times thicker than TBG, the difference between intralayer and interlayer Coulomb interactions may no longer be neglected, and thus we keep the layer dependence of Coulomb interactions, as manifested by the layer-index-dependent Coulomb interaction $V_{ll'}(\mathbf{q})$ [77],

$$V_{ll}(\mathbf{q}) = \frac{e^2}{2\Omega_0\epsilon_r\epsilon_0\sqrt{q^2+\kappa^2}},$$

$$V_{ll'}(\mathbf{q}) = \frac{e^2}{2\Omega_0\epsilon_r\epsilon_0 q}e^{-q|l-l'|d_0},\ l\neq l'. \tag{16}$$

A Thomas-Fermi-type screened Coulomb interaction is adopted for the intralayer Coulomb interaction $V_{ll}(\mathbf{q})$, with a fixed inverse screening length $\kappa = 0.0025$ Å^{-1} [77]. The interlayer Coulomb interaction $V_{ll'}(\mathbf{q})$ ($l \neq l'$) decays exponentially in momentum space with $d_0 = 3.35$ Å.

We then project the long-range Coulomb interactions onto the wave functions of the 3 conduction and 3 valence moiré bands of the renormalized continuum model [Eq. (14)], and perform unrestricted HF calculations within this 24-band (including valley and spin) low-energy window [77]. We have considered 32 trial initial states characterized by the order parameters $\{s_{0,z}\tau_a\sigma_b(a,b=x,y,z)\}$, where $\mathbf{s}$, $\boldsymbol{\tau}$, and $\boldsymbol{\sigma}$ denote Pauli matrices defined in the spin, valley, and sublattice subspaces, respectively. The background dielectric constant ϵ_r and displacement field D are treated as parameters, where $4 \leqslant \epsilon_r \leqslant 8$ and 0.7 V/nm $\leqslant D \leqslant 1.1$ V/nm. Here the only free parameter is ϵ_r, since D can be fixed by experiments. The screening of the displacement field has been treated self-consistently [77,80].

After projecting the Coulomb interaction to the renormalized low-energy wave functions, it can be written in the band basis

$$\hat{V}^{\rm intra} = \frac{1}{2N_s}\sum_{\widetilde{\mathbf{k}}\widetilde{\mathbf{k}}'\widetilde{\mathbf{q}}}\sum_{\substack{\mu\mu'\\ \sigma\sigma'\\ ll'}}\sum_{\substack{nm\\ n'm'}}\sum_{\mathbf{Q}} V_{ll'}(\mathbf{Q}+\widetilde{\mathbf{q}})\,\Omega^{\mu l,\mu' l'}_{nm,n'm'}(\widetilde{\mathbf{k}},\widetilde{\mathbf{k}}',\widetilde{\mathbf{q}},\mathbf{Q}) \times \hat{c}^\dagger_{\sigma\mu,n}(\widetilde{\mathbf{k}}+\widetilde{\mathbf{q}})\hat{c}^\dagger_{\sigma'\mu',n'}(\widetilde{\mathbf{k}}'-\widetilde{\mathbf{q}})\hat{c}_{\sigma'\mu',m'}(\widetilde{\mathbf{k}}')\hat{c}_{\sigma\mu,m}(\widetilde{\mathbf{k}}), \tag{17}$$

where the form factor $\Omega^{\mu l,\mu' l'}_{nm,n'm'}$ is expressed as

$$\Omega^{\mu l,\mu' l'}_{nm,n'm'}(\widetilde{\mathbf{k}},\widetilde{\mathbf{k}}',\widetilde{\mathbf{q}},\mathbf{Q}) = \sum_{\alpha\alpha'\mathbf{G}\mathbf{G}'} C^*_{\mu l\alpha\mathbf{G}+\mathbf{Q},n}(\widetilde{\mathbf{k}}+\widetilde{\mathbf{q}})C^*_{\mu' l'\alpha'\mathbf{G}'-\mathbf{Q},n'}(\widetilde{\mathbf{k}}'-\widetilde{\mathbf{q}}) \times C_{\mu' l'\alpha'\mathbf{G}',m'}(\widetilde{\mathbf{k}}')C_{\mu l\alpha\mathbf{G},m}(\widetilde{\mathbf{k}}). \tag{18}$$

The band indices n, m, n', m' run over the low-energy Hilbert space within E_C^* including 3 valence and 3 conduction bands (per spin per valley). $\{C_{\mu l\alpha\mathbf{G},m}(\widetilde{\mathbf{k}})\}$ denote the renormalized low-energy wave functions of band m at moiré wave vector $\widetilde{\mathbf{k}}$, where μ, l, α represent the valley, layer, and sublattice indices, respectively. $\mathbf{G}$, $\mathbf{G}'$, and $\mathbf{Q}$ denote the moiré reciprocal vectors, while $\widetilde{\mathbf{k}}$, $\widetilde{\mathbf{k}}'$, and $\widetilde{\mathbf{q}}$ denote wave vectors within the moiré Brillouin zone.

We make the Hartree-Fock approximation to Eq. (17) such that the two-particle Hamiltonian is decomposed into a superposition of the Hartree and Fock effective single-particle terms, where the Hartree term and the Fock term are expressed, respectively, as

$$\hat{V}_H^{\text{intra}} = \frac{1}{2N_s}\sum_{\widetilde{\mathbf{k}}\widetilde{\mathbf{k}}'}\sum_{\substack{\mu\mu'\\ \sigma\sigma'\\ ll'}}\sum_{\substack{nm\\ n'm'}}\left(\sum_{\mathbf{Q}} V_{ll'}(\mathbf{Q})\,\Omega^{\mu l,\mu' l'}_{nm,n'm'}(\widetilde{\mathbf{k}},\widetilde{\mathbf{k}}',0,\mathbf{Q})\right)$$
$$\times\left(\langle\hat{c}^\dagger_{\sigma\mu,n}(\widetilde{\mathbf{k}})\hat{c}_{\sigma\mu,m}(\widetilde{\mathbf{k}})\rangle\hat{c}^\dagger_{\sigma'\mu',n'}(\widetilde{\mathbf{k}}')\hat{c}_{\sigma'\mu',m'}(\widetilde{\mathbf{k}}') + \langle\hat{c}^\dagger_{\sigma'\mu',n'}(\widetilde{\mathbf{k}}')\hat{c}_{\sigma'\mu',m'}(\widetilde{\mathbf{k}}')\rangle\hat{c}^\dagger_{\sigma\mu,n}(\widetilde{\mathbf{k}})\hat{c}_{\sigma\mu,m}(\widetilde{\mathbf{k}})\right), \tag{19}$$

$$\hat{V}_F^{\text{intra}} = -\frac{1}{2N_s}\sum_{\widetilde{\mathbf{k}}\widetilde{\mathbf{k}}'}\sum_{\substack{\mu\mu'\\ \sigma\\ ll'}}\sum_{\substack{nm\\ n'm'}}\left(\sum_{\mathbf{Q}} V_{ll'}(\widetilde{\mathbf{k}}'-\widetilde{\mathbf{k}}+\mathbf{Q})\,\Omega^{\mu l,\mu' l'}_{nm,n'm'}(\widetilde{\mathbf{k}},\widetilde{\mathbf{k}}',\widetilde{\mathbf{k}}'-\widetilde{\mathbf{k}},\mathbf{Q})\right)$$
$$\times\left(\langle\hat{c}^\dagger_{\sigma\mu,n}(\widetilde{\mathbf{k}}')\hat{c}_{\sigma\mu',m'}(\widetilde{\mathbf{k}}')\rangle\hat{c}^\dagger_{\sigma\mu',n'}(\widetilde{\mathbf{k}})\hat{c}_{\sigma\mu,m}(\widetilde{\mathbf{k}}) + \langle\hat{c}^\dagger_{\sigma\mu',n'}(\widetilde{\mathbf{k}})\hat{c}_{\sigma\mu,m}(\widetilde{\mathbf{k}})\rangle\hat{c}^\dagger_{\sigma\mu,n}(\widetilde{\mathbf{k}}')\hat{c}_{\sigma\mu',m'}(\widetilde{\mathbf{k}}')\right). \tag{20}$$

In Fig. 1(d) we show the ground-state Hartree-Fock band structures at filling 1, with $D = 0.97$ V/nm and $\epsilon_r = 5$. We see that the highest occupied band marked in orange now is energetically separated from the other moiré bands. Moreover, this isolated flat band has a Chern number 1, desirable to realize FCI at fractional fillings. We also note that the HF gap at filling 1 divides the Hilbert space within E_C^* into the occupied and unoccupied subspaces, as marked in Fig. 1(d). Such a partition would allow us to consider the electron-doping problem with respect to charge neutrality as the hole-doping one with respect to the gap at filling 1.

We continue to explore the HF phase diagram at filling 1 in the (D, ϵ_r) parameter space. As shown in Fig. 2(a), the system stays in a Chern-number-1 ground state in a large region of parameter space, which gives rise to an isolated, Chern-number-1 flat band [see Fig. 1(d)]. In Fig. 2(b), we present the gap of the HF ground state at filling 1 in the (D, ϵ_r) parameter space, which varies from 7 to 29 meV, and becomes metallic with trivial topological properties in the upper right corner. In Fig. 2(c) we show the bandwidth of the isolated HF flat band, which varies from 6 meV to 34 meV. In Fig. 2(d) we present the normalized Berry-curvature standard deviation of the isolated flat Chern band emerging from the topologically nontrivial HF ground state, where a smaller value implies more resemblance with the lowest Landau level satisfying the Girvin-MacDonald-Platzman algebra [88]. Combining the Chern number, energy gap, bandwidth, and Berry-curvature standard deviation obtained from HF calculations, we conclude that $0.8\ \text{V/nm} < D < 1\ \text{V/nm}$ and $5 \leqslant \epsilon_r \leqslant 6$ may be the best regime to realize FCI at partial fillings.

V. FRACTIONAL CHERN INSULATORS

We further consider hole-doping the isolated Hartree-Fock flat band [see Fig. 1(d)], and explore the interacting ground states of this flat band and at hole-doping levels of 1/3, 2/5, 3/5, and 2/3 (corresponding to electron dopings of 2/3, 3/5, 2/5, and 1/3) in the parameter space of D and ϵ_r. As discussed above, there are two types of topologically distinct isolated flat bands which emerge from two competing HF ground states: the Chern-number-1 isolated flat band from the topological HF ground state, and the Chern-number-0 flat band from the topologically trivial HF ground state. We consider hole-doping the two types of topologically distinct flat bands

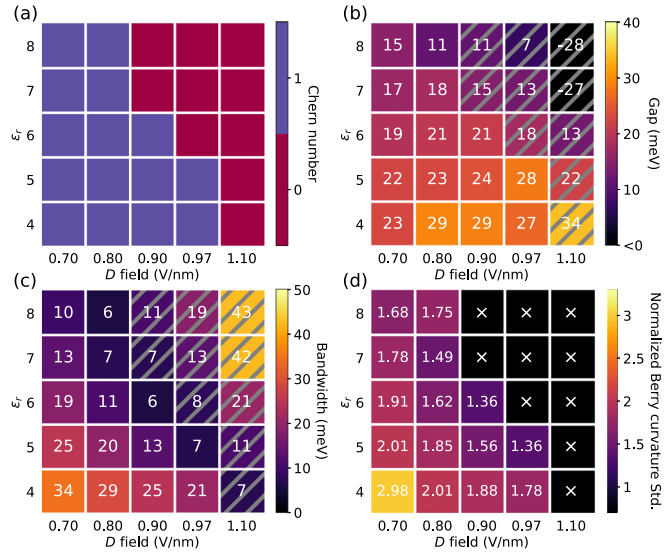

FIG. 2. Hartree-Fock phase diagram of hBN-PLG moiré superlattice at filling factor $\nu = 1$. (a) Chern number of the Hartree-Fock ground state, (b) gap of the Hartree-Fock ground state, (c) bandwidth of the isolated flat band right below the chemical potential (for $\nu = 1$), and (d) normalized Berry-curvature standard deviation of the flat Chern band right below chemical potential emerging from the topological HF ground state. The shaded regions in (b) and (c) mark the regions with topologically trivial ground states at $\nu = 1$.

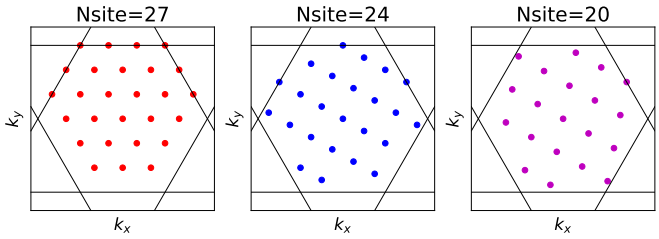

FIG. 3. Brillouin zone samplings for the ED calculations.

emerging from the two types of HF states, and determine the genuine many-body ground state.

A. Workflow for the ED calculations

Practically, we project the long-range *e-e* interactions [Eq. (15)] onto the wave functions of the isolated flat band emerging from the corresponding HF ground state at filling 1 ($\nu = 1$), and calculate the interacting ground states using ED under different hole-doping levels. Then, we compare their total energy to determine the genuine many-body ground state at given sets of parameters and doping levels.

In our numerical implementations, the exact-diagonalization (ED) calculations at 2/3 and 1/3 electron doping are performed on a 27-site cluster generated from three sets of 9-site clusters, and those at 3/5 and 2/5 electron doping are done on a 20-site (4×5) cluster. The spectral-flow calculations of (2/3, 1/3) and (3/5, 2/5) electron fillings are done on 24-site (4×6) and 20-site (4×5) clusters, respectively. The Brillouin zone samplings for the ED calculations are shown in Fig. 3. The Coulomb interactions in the ED calculations are identical to those adopted in the HF calculations in the previous subsection, which are then projected to the isolated flat band right below the chemical potential for HF states at filling 1, and the interacting ground states under different hole-doping levels are calculated using ED. Such an approach is justified as follows:

(i) First, we have set up a low-energy window E_C^* above which the effects of *e-e* interactions have been treated by perturbative RG, which leads to a *renormalized* low-energy effective model with its parameters given by Eq. (14). Such a renormalized continuum model applies to the low-energy cutoff $E_C^* \sim 150$ meV including 3 valence bands and 3 conduction bands per spin per valley, as shown in Fig. 1(b).

(ii) Second, within E_C^*, *e-e* Coulomb interactions can no longer be treated by perturbations. Instead, we first perform HF calculations at some integer filling ν, which divides the low-energy Hilbert space within E_C^* into the occupied and unoccupied subspaces, as shown in Fig. 1(d). The integer filling factor ν is made in such a way that the occupied and unoccupied subspaces are well separated by a gap. In the present study, we make the choice $\nu = 1$ [see Fig. 1(d)]. The presence of such a gap at $\nu = 1$ is not only theoretically confirmed by HF calculations, but also justified by the experimental observation of robust integer quantum Hall effect at filling 1 over a large range of D field (0.75 V/nm $\lessapprox D \lessapprox 1.1$ V/nm) in the system [5].

(iii) Third, we further consider either hole-doping the occupied subspace with respect to the gap at $\nu = 1$ or electron-doping the unoccupied subspace with respect to the gap at $\nu = 0$. This requires the projection of the Coulomb interactions onto either the occupied or unoccupied HF wave functions within E_C^*. Then, in principle, one needs to perform *multiband* ED calculations within either subspace. For the case of $\nu = 1$, there are 13 occupied bands and 11 unoccupied bands within E_C^* as shown in Fig. 1(d). Thus, in principle one needs to do a 13-band ED calculation if considering hole-doping the $\nu = 1$ HF ground state.

(iv) Performing a 13-band ED calculation is certainly unrealistic. Nevertheless, we note that within the occupied subspace at $\nu = 1$, the highest occupied HF band originates from the spin-valley polarized first moiré conduction band, which is well separated from the valence moiré bands by a single-particle gap ~80–100 meV at large D fields, as shown in Fig. 1(d), which is greater than the *e-e* Coulomb interaction energy scale in the system (~20 meV). Thus, when hole-doping the highest occupied HF band with respect to $\nu = 1$, it is legitimate to freeze the 12 occupied valence moiré bands and project Coulomb interactions only to the isolated, spin-valley polarized conduction flat band, which is highlighted in orange in Fig. 1(d).

(v) It is worthwhile noting that the choice of integer filling ν is not unique. Another natural choice is $\nu = 0$, which divides the low-energy Hilbert space E_C^* into 12 occupied bands and 12 unoccupied bands. With such a choice, one needs to electron-dope the unoccupied subspace. However, since the 12 unoccupied bands are entangled together [see Fig. 1(c)], one has to project Coulomb interactions onto all of the 12 unoccupied bands and perform 12-band ED calculation, which is barely possible. So the best choice is to hole-dope the $\nu = 1$ HF ground state.

(vi) Nevertheless, we note that HF calculations may overestimate the energy gap; thus in reality the occupied topological flat band emerging from the Chern-insulator state at filling 1 may be closer in energy to the unoccupied states. Moreover, the relevant low-energy Hilbert space may vary with filling factors, such that the low-energy Hilbert space for the FCI states at fractional fillings may be different from that at filling 1. In either case, one needs to consider multiple bands when performing the ED calculations, which is beyond the scope of the present study.

B. Results at 1/3 and 2/3 fillings

With the workflow sketched above, in the end we only need to perform ED calculations within an isolated moiré band from one spin one valley which is right below the chemical potential of HF state at filling 1. However, we need to perform ED calculations at partial hole fillings with respect to two types of topologically distinct HF states at $\nu = 1$. For the topological nontrivial HF state, an isolated flat band with Chern number 1 is generated, while for the topological trivial case, a flat band with zero Chern number is obtained. These two HF states are competing with each other with energy difference ~0.01–1 meV. Therefore, one needs to hole dope both types of isolated flat bands, and compare the energies of the many-body ground states in the two cases. One needs to be

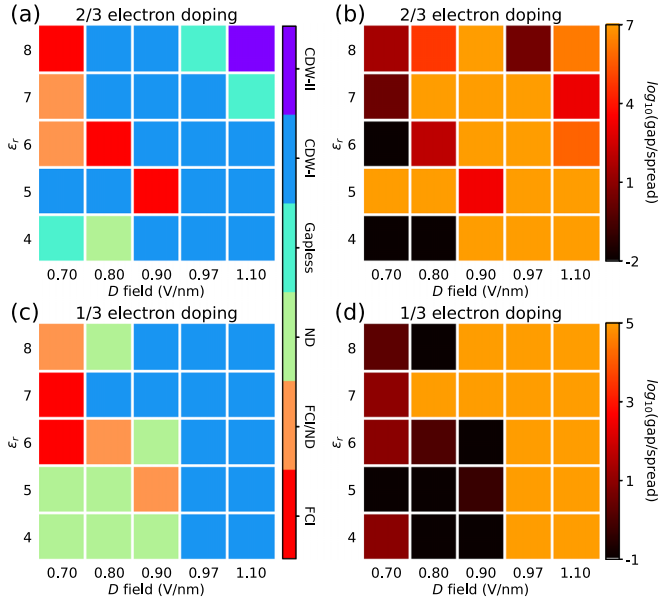

FIG. 4. Phase diagram at 2/3 and 1/3 electron fillings obtained from exact-diagonalization calculations. (a) Phase diagram at 2/3 electron filling, (b) the "gap/spread" (see text) at 2/3 electron filling plotted on a logarithmic scale, (c) phase diagram at 1/3 electron filling, and (d) the "gap/spread" at 1/3 electron filling plotted on a logarithmic scale. In (a) and (c), "FCI" stands for fractional Chern insulator, "ND" stands for nondegenerate state, "CDW" stands for charge density wave, while "FCI/ND" denotes crossover state between FCI and ND.

careful that, when performing the particle-hole transformation $\hat{c}_{\mathbf{k}} \to \hat{h}^{\dagger}_{-\mathbf{k}}$ (where $\hat{c}_{\mathbf{k}}$ refers to electron annihilation operator and $\hat{h}^{\dagger}_{-\mathbf{k}}$ refers to hole creation operator), the two-particle interaction Hamiltonian Eq. (15) is unchanged. However, the single-particle Hamiltonian is changed by a constant due to normal ordering of the hole operators, i.e.,

$$\hat{c}^{\dagger}_{\mathbf{k}}\,\hat{c}_{\mathbf{k}} \to \hat{h}_{-\mathbf{k}}\,\hat{h}^{\dagger}_{-\mathbf{k}} = 1 - \hat{h}^{\dagger}_{-\mathbf{k}}\,\hat{h}_{-\mathbf{k}}. \tag{21}$$

Thus, the effective single-particle Hamiltonian of the isolated flat band generated from the $\nu = 1$ HF state is also subjected to the above transformation:

$$\hat{H}^{\mathrm{HF}}_{\nu=1} = \sum_{\mathbf{k}} E^{\mathrm{HF}}_{\mathbf{k}}\,(1 - \hat{h}^{\dagger}_{-\mathbf{k}}\,\hat{h}_{-\mathbf{k}}), \tag{22}$$

where $E^{\mathrm{HF}}_{\mathbf{k}}$ is the valley-spin polarized HF energy dispersion of the isolated flat band right below the chemical potential of the $\nu = 1$ HF state, and $\mathbf{k}$ is the wave vector within the moiré Brillouin zone. We note that in order to compare the energies of many-body states at partial hole fillings of two different HF flat bands, one has to include the constant HF band energy sum in Eq. (22), which may be interpreted as "effective vacuum energy" of the two different HF vacua in our calculations.

Keeping this subtlety in mind, at 2/3 electron doping (1/3 hole doping), we perform ED calculations on a 27-site cluster with periodic boundary condition (see Fig. 3), and dope 9 holes into the two types of isolated flat band. The phase diagram at 2/3 electron filling is shown in Fig. 4(a). We see that Laughlin-type FCI state (marked in red) is fiercely competing with two types of CDW states (marked by "CDW1" in blue and "CDW2" in purple) and a nondegenerate state ("ND" marked in light green). Both the FCI state and the CDW states are characterized by a (nearly) threefold-degenerate ground-state manifold, which is separated from other excited states by a finite energy gap on the order of 1–10 meV. The ND, however, is characterized by a nondegenerate ground state separated from excited states by a gap on the order of 1 meV. We note that there are three blocks in the (D, ϵ_r) space exhibiting the FCI ground state at 2/3 filling, i.e., ($\epsilon_r = 5$, $D = 0.9$ V/nm), ($\epsilon_r = 6$, $D = 0.8$ V/nm), and ($\epsilon_r = 8$, $D = 0.7$ V/nm), as indicated by red color in Fig. 4(a). Moreover, it is interesting to note that there is also a finite region in the phase diagram of Fig. 4(a) in which the system seems to undergo a crossover from a nondegenerate state to FCI. Such a crossover region is marked as "FCI/ND" by orange color in Fig. 4(a). The presence of such a crossover regime may be attributed to finite-size effects. In the thermodynamics limit, the crossover regime is expected to shrink to a line of phase boundary.

In order to better capture the characters of the different types of many-body states shown in the phase diagram at 2/3 electron filling, we extract the energy gap between the fourth and third eigenstates, and divide it by the energy spread of the first three lowest-energy eigenstates. Such "gap/spread" function is plotted in (D, ϵ_r) space on a logarithmic scale, as shown in Fig. 4(b). If the log of this quantity is large, it means that there are three low-energy states which are separated from the fourth state by a notable gap, which implies either FCI or CDW state. Otherwise, it could either be a gapless state or a ND state. Practically, in our calculations a threefold quasidegenerate many-body state is identified as a FCI if it is topologically nontrivial (to be discussed in the following) and meanwhile the log of its gap/spread is greater than 0.5. We find that the log of this gap/spread quantity is largest (∼4) at $D = 0.9$ V/nm and $\epsilon_r = 5$, which means that the FCI state around this point is most stable. More detailed characterizations of the different types of correlated states are to be discussed later.

In Fig. 4(c) we present the phase diagram at 1/3 electron filling. The FCI ground state emerges at ($D = 0.7$ V/nm, $\epsilon_r = 6$) and ($D = 0.7$ V/nm, $\epsilon_r = 7$). However, experimentally no signature of the fractional quantum anomalous Hall effect has been observed at 1/3 electron filling, while it is observed for 0.95 V/nm $\lessapprox D \lessapprox$ 0.965 V/nm at 2/3 filling [5]. Comparing our theoretical results with experimental observations at both 2/3 and 1/3 fillings, we find that the background dielectric constant can be unambiguously determined as $\epsilon_r = 5$, which leads to results that are consistent with experiments at both fillings. In Sec. V C, we will show that using the same dielectric constant $\epsilon_r = 5$, we are also able to obtain numerical results that are quantitatively consistent with experimental observations at 3/5 and 2/5 fillings. In Fig. 4(d) we present the "gap/spread" (as defined above) at 1/3 filling on a logarithmic scale. Clearly, the CDW region is marked by large and positive "$\log_{10}$(gap/spread)" value ∼5, while the FCI region has a small value ∼0.5–1, much smaller than that of the FCI state at 2/3 filling (∼2–4). This indicates that the FCI state obtained at 1/3 filling for $D = 0.7$ V/nm and $\epsilon_r = 6, 7$ is not as robust as that at 2/3 filling. Again, here we identify a threefold-

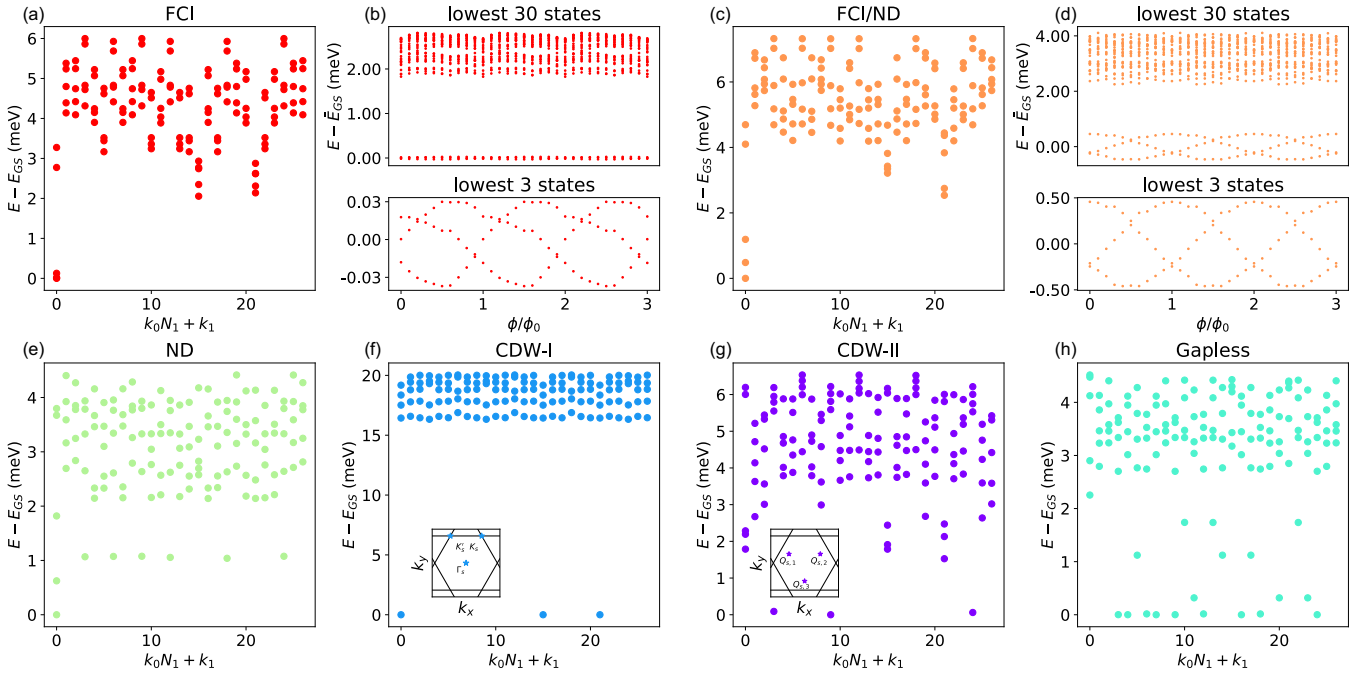

FIG. 5. (a) Many-body band structures of Laughlin-type fractional Chern insulator state at 2/3 electron doping. (b) The spectral-flow behavior of Laughlin-type FCI state, where the upper panel shows the spectral flow of the lowest 30 states, and the lower panel zooms in the spectral flow within the (nearly) threefold-degenerate ground-state manifold. (c) Many-body band structures of a crossover state between fractional Chern insulator and nondegenerate state (FCI/ND), which shows three low-lying states separated by a gap from other excited states. But the gap is comparable to the energy spread of the three low-lying states. (d) Spectral-flow behavior of the crossover FCI/ND state. (e) Many-body band structures of nondegenerate state. Many-body band structures of (f) CDW1 state and (g) CDW2 state, where their insets mark the ground-state crystalline momenta within moiré Brillouin zone. (h) Many-body band structures of the gapless phase.

quasidegenerate state as FCI if it is topologically nontrivial (to be discussed later) and if the log of its gap/spread quantity is greater than 0.5.

As mentioned above, both FCI and CDW states are characterized by (nearly) threefold-degenerate ground states and finite energy gaps. One has to look at more detailed properties to distinguish them. To this end, in Fig. 5 we show the total energy versus total crystalline momenta dispersions (dubbed as "many-body band structures" hereafter) of various types of correlated states. In particular, as shown in Fig. 5(a), the many-body band structures of FCI exhibits three (nearly) degenerate ground states in the zero-momentum sector, which satisfies the "generalized Pauli principle" [6] for 27 sites at 1/3 hole doping. Upon the adiabatic insertion of magnetic flux ϕ, the three degenerate ground states of FCI would flow into each other, and come back to the original configuration when $\phi = 3\phi_0$ ($\phi_0 = h/e$ is the flux quantum). With Landau gauge, this amounts to changing the crystalline momentum along one direction by $\delta k_1 = (\phi/\phi_0)/N_1$, where N_i ($i = 1, 2$) is the number of lattice sites along the two primitive reciprocal vector directions, and k_1 is the corresponding reduced crystalline momentum along the first reciprocal vector direction. Such spectral-flow behavior of the FCI state at 2/3 electron filling is clearly shown in the lower panel of Fig. 5(b). For the purpose of spectral-flow calculation at 2/3 electron filling, we take a 4×6 site with 8 holes (see Fig. 3), which also yields the FCI state the same as the case of 27 sites and 9 holes.

In Fig. 5(c) we present the typical many-body band structures of the FCI/ND crossover states at 2/3 electron filling. We see that, although there are three low-lying states which are separated from the fourth state by a gap ∼1 meV, the energy spread of the three low-lying states is also about 1 meV. In Fig. 5(d) we show the energy of the FCI/ND crossover state as a function of inserted fluxes (for 24-site system with 8 holes). There is similar spectral-flow behavior as FCI. Nevertheless, the large energy spread of the three low-lying states and small excitation gap hinder us from calling it FCI. In Fig. 5(e) we present the many-body band structures of the ND state, which clearly show a nondegenerate ground state.

In Figs. 5(f) and 5(g), we show typical many-body band structures of the two types of CDW states. Both types of CDW states are threefold degenerate and are gapped from the excited states. However, for the first type of CDW (CDW1), the total crystalline momenta of the three ground states occur at Γ_s, K_s, and K_s' as marked in the inset of Fig. 5(f), which are the characteristic wave vectors of CDW states at 1/3 and 2/3 fillings preserving threefold rotational symmetry. For the second type of CDW (CDW2), the total reduced crystalline momenta of the three degenerate ground states are (0, 1/3), (1/3, 0), and (2/3, 2/3), as marked in the inset of Fig. 5(g). The CDW2 state is a stripe state that breaks the threefold rotational symmetry. In Fig. 5(h), typical many-body band structures for the gapless phase are also presented.

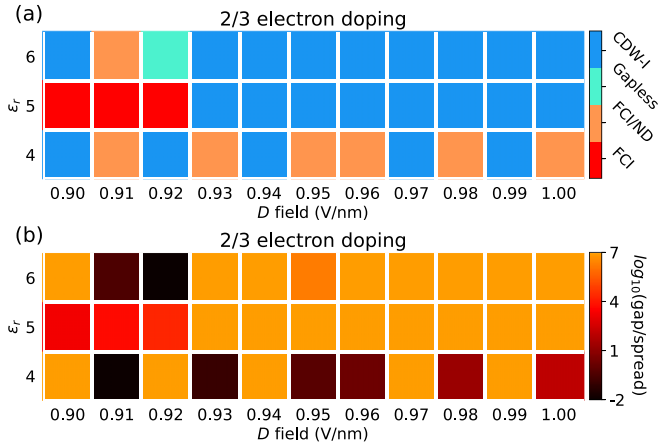

FIG. 6. (a) Finer phase diagrams in a smaller range of parameters 0.9 V/nm $\leqslant D \leqslant$ 1.0 V/nm and $4 \leqslant \epsilon_r \leqslant 6$ at 2/3 electron filling. (b) The corresponding "gap/spread" (see text) at 2/3 electron filling plotted on a logarithmic scale.

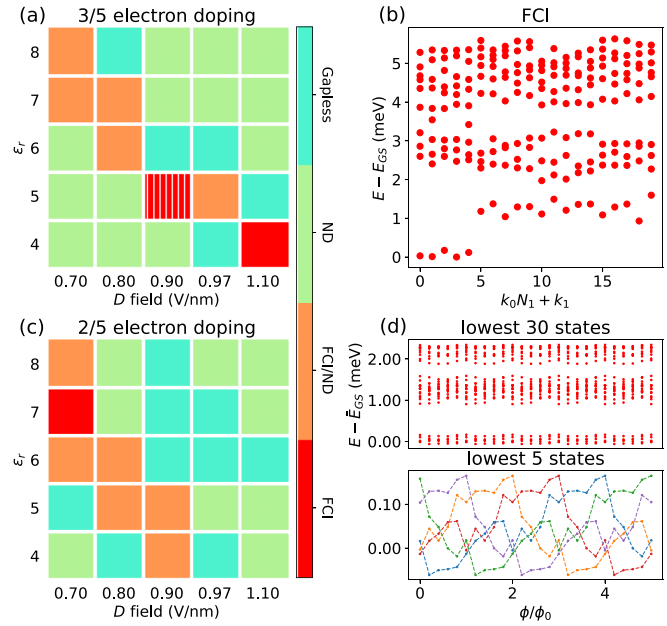

FIG. 7. Phase diagram and many-body energy spectra at 3/5 and 2/5 electron fillings obtained from exact-diagonalization calculations. (a) Phase diagram at 3/5 electron filling. (b) Many-body band structures of the composite-fermion type FCI state at 3/5 electron filling at $D = 0.94$ V/nm and $\epsilon_r = 5$. (c) Phase diagram at 2/5 electron filling. (d) Spectral-flow behavior of the composite-fermion type FCI state at 3/5 electron filling, where the upper panel shows the spectral flow of lowest 30 states, while the lower panel zooms in on the spectral flow within the (nearly) fivefold-degenerate ground-state manifold. The fine white mesh within the red FCI block in (a) means that we have performed ED calculations in a finer range of D field at 3/5 electron filling for 0.9 V/nm $\leqslant D \leqslant$ 0.96 V/nm (with interval of 0.1 V/nm) at $\epsilon_r = 5$.

We continue to search for the phase diagram at 2/3 electron filling (1/3 hole filling) within a smaller parameter space 0.9 V/nm $\leqslant D \leqslant$ 1.0 V/nm and $4 \leqslant \epsilon_r \leqslant 6$, and we compare the ground-state energies by 1/3 hole doping to topologically distinct flat bands derived from two competing HF states at $\nu = 1$. This finer phase diagram is presented in Fig. 6(a). When 0.9 V/nm $\leqslant D \leqslant$ 0.92 V/nm and $\epsilon_r = 5$, FCI is the ground state at 2/3 electron filling. In Fig. 6(b) we present the "gap/spread" on a logarithmic scale, which shows peak values in the FCI and CDW states. It is worthwhile noting that the experimentally fractional quantum anomalous Hall effect shows up at 2/3 filling for 0.95 V/nm $\lessapprox D \lessapprox$ 0.965 V/nm [5], which is quantitatively consistent with the fine phase diagram in Fig. 6(a).

C. Results at 2/5 and 3/5 fillings

We further consider the situations of 2/5 and 3/5 hole dopings of the isolated flat band with respect to $\nu = 1$, corresponding to 3/5 and 2/5 electron dopings with respect to the charge neutrality point. We perform ED calculations on a 20-site (4×5; see Fig. 3) cluster under periodic boundary conditions with 8 (2/5 hole doping) and 12 (3/5 hole doping) doped holes. The fractional quantum anomalous Hall effect has been observed at both of these fillings [5], implying the presence of composite-fermion-type FCI states [23] at these fillings. In Fig. 7 we present the phase diagram at 3/5 electron filling, which is obtained by 2/5-hole-doping the two types of isolated flat bands emerging from the two competing HF states at $\nu = 1$. We see that when $D = 0.9$ V/nm and $\epsilon_r = 5$, and $D = 1.1$ V/nm and $\epsilon_r = 4$, the system may stay in composite-fermion-type FCI state marked by red blocks in Fig. 7(a). The fine white mesh within the red FCI block at ($D = 0.9$ V/nm, $\epsilon_r = 5$) in Fig. 7(a) means that within this red block, we have performed ED calculations in a finer range of D field at 2/5 hole filling (3/5 electron filling) of the two distinct flat bands emerging from the two competing HF states at filling 1. We find that the system stays in the composite-fermion FCI state for $D = 0.9$ V/nm and for $D = 0.93$ V/nm $\leqslant D \leqslant$ 0.95 V/nm (with interval of 0.1 V/nm) with $\epsilon_r = 5$. Such a state is characterized by a fivefold (nearly) degenerate ground state and a sizable gap ~1 meV from the excited states, as shown in Fig. 7(b). Moreover, upon the adiabatic flux insertion, these five nearly degenerate ground states would interchange with each other and return to the original configurations when $\phi = 5\phi_0$, as clearly shown in Fig. 7(d). This further confirms the topological nature of such a degenerate many-body state. There are also some other correlated ground states in the (D, ϵ_r) phase diagram at 3/5 electron filling, such as the ND, gapless, and FCI/ND crossover states, as shown in Fig. 7(a).

In contrast, at 2/5 electron filling, according to our ED calculation on a relatively rough mesh in the (D, ϵ_r) space as shown in Fig. 7(c), the FCI state only shows up at $D =$ 0.7 V/nm and $\epsilon_r = 7$. And this FCI state is not very robust, with the log of the gap/spread ~1.18. When $\epsilon_r = 5$, the FCI/ND crossover state emerges for $D = 0.8, 0.9$ V/nm at 2/5 electron filling. We note that in experiments the fractional quantum anomalous Hall effect has been observed over a relatively large range of D field at 3/5 filling (0.91 V/nm $\lessapprox D \lessapprox$ 0.95 V/nm), but only observed within a small range of D field at 2/5 filling (0.92 V/nm $\lessapprox D \lessapprox$ 0.93 V/nm) [5]. Therefore,

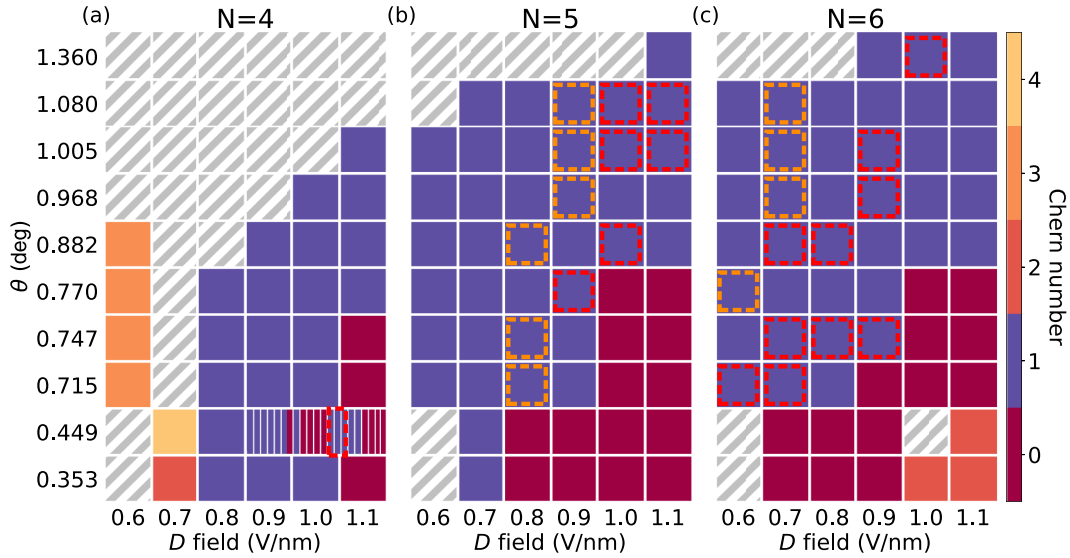

FIG. 8. Phase diagrams at 2/3 electron filling, for (a) tetralayer, (b) pentalayer, and (c) hexalayer graphene moiré superlattice aligned with hBN. The FCI (FCI/ND) states are marked by red (orange) dashed boxes. The color coding indicates Chern numbers of the isolated flat bands emerging from gapped HF ground states at filling 1, where the gray shaded regions mark the gapless states. The dense narrow color bars (representing Chern numbers) in (a) at 0.449° represent a fine scanning of D field from 0.9 V/nm to 1.1 V/nm with an interval of 0.01 V/nm.

our numerical results with $\epsilon_r = 5$ at 2/5 and 3/5 fillings are also fully consistent with experimental observations.

VI. GENERIC MULTILAYER GRAPHENE SYSTEMS

We further apply our theoretical formalism to generic rhombohedral multilayer graphene systems with only their bottom layers aligned with hBN, and have established many-body phase diagrams for various multilayer systems in the parameter space of twist angle θ and D field, with fixed dielectric constant $\epsilon_r = 5$. In Figs. 8(a), 8(b) and 8(c), we present the Chern number of the lowest conduction bands (LCBs) (with respect to the charge neutral point) obtained from the interaction-driven symmetry-breaking ground states at $\nu = 1$ under the HF approximation for $N = 4$, 5, and 6, respectively. An ill-defined Chern number is marked with shaded area implying that the direct gap between the first and second conduction bands is vanishingly small. It is interesting to note that in most parts of the parameter space, the Hartree-Fock LCBs exhibit Chern number 1 for $N = 4, 5$, and 6. Our calculations indicate that the integer Chern insulator state is robust in tetralayer, pentalayer, and hexalayer graphene moiré superlattices at filling factor 1.

For the $N = 4$ system, we have performed exact-diagonalization calculations at 1/3 hole filling of the Chern-number-1 LCB emerging from symmetry-breaking Hartree-Fock states (corresponding to 2/3 electron filling with respect to charge neutrality), and find that FCI state is stable only at ($D = 1.02$–1.04 V/nm, $\theta = 0.449°$), as marked by a narrow red dashed box in Fig. 8(a), where the dense narrow color bars (representing Chern numbers) in Fig. 8(a) at 0.449° represent a fine scanning of D field from 0.9 V/nm to 1.1 V/nm with an interval of 0.01 V/nm. For the $N = 5$, i.e., pentalayer, system, we find that the FCI state is stable in a substantial region of the (D, θ) parameter space as marked by red dashed boxes in Fig. 8(b). Moreover, there is also some region in the (D, θ) parameter space which exhibits a crossover between the FCI and nondegenerate states (dubbed as FCI/ND), marked by orange dashed boxes in Fig. 8(b). Lastly, for the $N = 6$ system, the bandwidth of the topological LCB emerging from the symmetry-breaking Hartree-Fock states at filling 1 is comparable to that of the $N = 5$ system, while the corresponding Berry-curvature standard deviations are even smaller than those of the $N = 5$ system (see Supplemental Material [77]). Therefore, one would expect that the FCI state may be even more robust for the $N = 6$ system at fractional fillings. In Fig. 8(c) the FCI ground state in the $N = 6$ system is marked by red dashed boxes in the phase diagram, and the orange dashed boxes in Fig. 8(c) mark the FCI/ND state.

Overall, for the tetralayer system ($N = 4$), the integer Chern insulator state exists over a finite range of twist angles and D fields at filling 1, while the fractional Chern insulator only exists at $\theta = 0.449°$ in an extremely small range of D (1.02 V/nm $\leqslant D \leqslant 1.04$ V/nm). For pentalayer and hexalayer systems ($N = 5$ and $N = 6$), both integer and fractional Chern insulators are present, and exist over a finite range of twist angles and D fields. For the hexalayer system, the normalized Berry curvature standard deviations of the topological LCBs (emerging from the Hartree-Fock ground states filling 1) are even smaller than those of the pentalayer system, which may imply more stable FCI ground states at fractional fillings. More details can be found in the Supplemental Material [77].

VII. CONCLUSIONS

To some extent, our theory can be considered as being developed from first principles. We start from the highest energy scale $E_C \sim 2$ eV in the problem and progressively integrate out the high-energy modes using RG until a low-energy cutoff $E_C^* \sim 0.15$ eV is reached. We thus obtain a renormalized low-energy Hamiltonian including the effects of Coulomb

TABLE I. The range of D (in units of V/nm) within which the fractional quantum anomalous Hall effect shows up. We show the results from our theoretical calculations with $\epsilon_r = 5$, and the experimental observations [5].

	Filling			
	2/3	1/3	3/5	2/5
Theory	$0.9 \leqslant D \leqslant 0.92$	None	$0.9 \leqslant D \leqslant 0.95$	None
Experiment	$0.95 \lessapprox D \lessapprox 0.965$	None	$0.91 \lessapprox D \lessapprox 0.95$	$0.92 \lessapprox D \lessapprox 0.93$

interactions from remote-band electrons to low-energy electrons, with self-consistently screened D field. Within E_C^*, we perform fully unrestricted HF calculations at filling 1, which yield two competing HF states with distinct topological characters. We further compare the energies of ED ground states by hole-doping the topologically distinct flat bands emerging from two competing HF states, and determine the genuine many-body ground state. Eventually, we obtain FCI states at both 2/3 and 3/5 fillings with $\epsilon_r = 5$ for the PLG system, which emerge in a range of D fields that are quantitatively consistent with experiments as shown in Table I. Our work thus provides a microscopic theory for the fractional quantum anomalous Hall effect and other correlated states observed in the hBN-PLG moiré superlattice.

We have theoretically studied the correlated topological states in generic hBN-aligned N-layer graphene moiré superlattices (with $N = 2, 3, 4, 5, 6$), where many-body phase diagrams have also been constructed in the parameter space of D (0.6 V/nm $\leqslant D \leqslant 1.1$ V/nm) and θ ($0.353^\circ \leqslant \theta \leqslant 1.36^\circ$). We find that a robust FCI state at 2/3 electron filling may emerge in both pentalayer and hexalayer systems. For the tetralayer graphene moiré superlattice, the integer Chern insulator state is robust at filling factor 1, while FCI at 2/3 filling occurs only within a small range of D field around 1 V/nm at twist angle $\theta = 0.449^\circ$. The methodology developed in this work can be readily applied to various other two-dimensional systems to explore potentially richer correlated and topological physics.

Note added. Recently, we became aware of several closely related works [89–92].

ACKNOWLEDGMENTS

We thank Yang Zhang, Zhengguang Lu, and Jiabin Yu for helpful discussions. This work is supported by the National Key R&D Program of China (Grant No. 2020YFA0309601), the National Natural Science Foundation of China (Grant No. 12174257), the Science and Technology Commission of Shanghai Municipality (Grant No. 21JC1405100), and a start-up grant from ShanghaiTech University.

[1] H. Park, J. Cai, E. Anderson, Y. Zhang, J. Zhu, X. Liu, C. Wang, W. Holtzmann, C. Hu, Z. Liu, T. Taniguchi, K. Watanabe, J.-H. Chu, T. Cao, L. Fu, W. Yao, C.-Z. Chang, D. Cobden, D. Xiao, and X. Xu, Nature (London) **622**, 74 (2023).

[2] F. Xu, Z. Sun, T. Jia, C. Liu, C. Xu, C. Li, Y. Gu, K. Watanabe, T. Taniguchi, B. Tong, J. Jia, Z. Shi, S. Jiang, Y. Zhang, X. Liu, and T. Li, Phys. Rev. X **13**, 031037 (2023).

[3] J. Cai, E. Anderson, C. Wang, X. Zhang, X. Liu, W. Holtzmann, Y. Zhang, F. Fan, T. Taniguchi, K. Watanabe, Y. Ran, T. Cao, L. Fu, D. Xiao, W. Yao, and X. Xu, Nature (London) **622**, 63 (2023).

[4] Y. Zeng, Z. Xia, K. Kang, J. Zhu, P. Knüppel, C. Vaswani, K. Watanabe, T. Taniguchi, K. F. Mak, and J. Shan, Nature (London) **622**, 69 (2023).

[5] Z. Lu, T. Han, Y. Yao, A. P. Reddy, J. Yang, J. Seo, K. Watanabe, T. Taniguchi, L. Fu, and L. Ju, Nature (London) **626**, 759 (2024).

[6] N. Regnault and B. A. Bernevig, Phys. Rev. X **1**, 021014 (2011).

[7] D. N. Sheng, Z.-C. Gu, K. Sun, and L. Sheng, Nat. Commun. **2**, 389 (2011).

[8] T. Neupert, L. Santos, C. Chamon, and C. Mudry, Phys. Rev. Lett. **106**, 236804 (2011).

[9] E. Tang, J.-W. Mei, and X.-G. Wen, Phys. Rev. Lett. **106**, 236802 (2011).

[10] K. Sun, Z. Gu, H. Katsura, and S. Das Sarma, Phys. Rev. Lett. **106**, 236803 (2011).

[11] G. Möller and N. R. Cooper, Phys. Rev. Lett. **103**, 105303 (2009).

[12] X.-L. Qi, Phys. Rev. Lett. **107**, 126803 (2011).

[13] D. C. Tsui, H. L. Stormer, and A. C. Gossard, Phys. Rev. Lett. **48**, 1559 (1982).

[14] R. B. Laughlin, Phys. Rev. Lett. **50**, 1395 (1983).

[15] J. K. Jain, Phys. Rev. Lett. **63**, 199 (1989).

[16] G. Moore and N. Read, Nucl. Phys. B **360**, 362 (1991).

[17] H. L. Stormer, D. C. Tsui, and A. C. Gossard, Rev. Mod. Phys. **71**, S298 (1999).

[18] R. E. Prange and S. M. Girvin, *The Quantum Hall Effect* (Springer, New York, NY, 2012).

[19] Y.-F. Wang, Z.-C. Gu, C.-D. Gong, and D. N. Sheng, Phys. Rev. Lett. **107**, 146803 (2011).

[20] Y.-L. Wu, B. A. Bernevig, and N. Regnault, Phys. Rev. B **85**, 075116 (2012).

[21] Z. Liu, E. J. Bergholtz, H. Fan, and A. M. Läuchli, Phys. Rev. Lett. **109**, 186805 (2012).

[22] J. W. F. Venderbos, S. Kourtis, J. van den Brink, and M. Daghofer, Phys. Rev. Lett. **108**, 126405 (2012).

[23] T. Liu, C. Repellin, B. A. Bernevig, and N. Regnault, Phys. Rev. B **87**, 205136 (2013).

[24] X. Hu, M. Kargarian, and G. A. Fiete, Phys. Rev. B **84**, 155116 (2011).

[25] R. Roy, Phys. Rev. B **90**, 165139 (2014).

[26] M. Claassen, C. H. Lee, R. Thomale, X.-L. Qi, and T. P. Devereaux, Phys. Rev. Lett. **114**, 236802 (2015).

[27] J. Wang, J. Cano, A. J. Millis, Z. Liu, and B. Yang, Phys. Rev. Lett. **127**, 246403 (2021).
[28] P. J. Ledwith, A. Vishwanath, and D. E. Parker, Phys. Rev. B **108**, 205144 (2023).
[29] D. Bauer, S. Talkington, F. Harper, B. Andrews, and R. Roy, Phys. Rev. B **105**, 045144 (2022).
[30] B. Andrews, M. Raja, N. Mishra, M. Zaletel, and R. Roy, Phys. Rev. B **109**, 245111 (2024).
[31] R. Bistritzer and A. H. MacDonald, Proc. Natl. Acad. Sci. USA **108**, 12233 (2011).
[32] G. Tarnopolsky, A. J. Kruchkov, and A. Vishwanath, Phys. Rev. Lett. **122**, 106405 (2019).
[33] Z. Song, Z. Wang, W. Shi, G. Li, C. Fang, and B. A. Bernevig, Phys. Rev. Lett. **123**, 036401 (2019).
[34] J. Liu, J. Liu, and X. Dai, Phys. Rev. B **99**, 155415 (2019).
[35] J. Ahn, S. Park, and B.-J. Yang, Phys. Rev. X **9**, 021013 (2019).
[36] H. C. Po, L. Zou, T. Senthil, and A. Vishwanath, Phys. Rev. B **99**, 195455 (2019).
[37] N. Bultinck, S. Chatterjee, and M. P. Zaletel, Phys. Rev. Lett. **124**, 166601 (2020).
[38] J. Wang, Y. Zheng, A. J. Millis, and J. Cano, Phys. Rev. Res. **3**, 023155 (2021).
[39] Z.-D. Song, B. Lian, N. Regnault, and B. A. Bernevig, Phys. Rev. B **103**, 205412 (2021).
[40] Z.-D. Song and B. A. Bernevig, Phys. Rev. Lett. **129**, 047601 (2022).
[41] H. Shi and X. Dai, Phys. Rev. B **106**, 245129 (2022).
[42] Y.-H. Zhang, D. Mao, and T. Senthil, Phys. Rev. Res. **1**, 033126 (2019).
[43] B. L. Chittari, G. Chen, Y. Zhang, F. Wang, and J. Jung, Phys. Rev. Lett. **122**, 016401 (2019).
[44] Y. Park, Y. Kim, B. L. Chittari, and J. Jung, Phys. Rev. B **108**, 155406 (2023).
[45] T. Han, Z. Lu, G. Scuri, J. Sung, J. Wang, T. Han, K. Watanabe, T. Taniguchi, L. Fu, H. Park, and L. Ju, Nature (London) **623**, 41 (2023).
[46] T. Han, Z. Lu, G. Scuri, J. Sung, J. Wang, T. Han, K. Watanabe, T. Taniguchi, H. Park, and L. Ju, Nat. Nanotechnol. **19**, 181 (2024).
[47] J. Liu, Z. Ma, J. Gao, and X. Dai, Phys. Rev. X **9**, 031021 (2019).
[48] M. Koshino, Phys. Rev. B **99**, 235406 (2019).
[49] J. Y. Lee, E. Khalaf, S. Liu, X. Liu, Z. Hao, P. Kim, and A. Vishwanath, Nat. Commun. **10**, 5333 (2019).
[50] F. Haddadi, Q. Wu, A. J. Kruchkov, and O. V. Yazyev, Nano Lett. **20**, 2410 (2020).
[51] P. J. Ledwith, A. Vishwanath, and E. Khalaf, Phys. Rev. Lett. **128**, 176404 (2022).
[52] J. Wang and Z. Liu, Phys. Rev. Lett. **128**, 176403 (2022).
[53] B. Xie, R. Peng, S. Zhang, and J. Liu, npj Comput. Mater. **8**, 110 (2022).
[54] P. J. Ledwith, E. Khalaf, Z. Zhu, S. Carr, E. Kaxiras, and A. Vishwanath, arXiv:2111.11060.
[55] Z. Ma, S. Li, Y.-W. Zheng, M.-M. Xiao, H. Jiang, J.-H. Gao, and X. Xie, Sci. Bull. **66**, 18 (2021).
[56] S. Zhang, B. Xie, Q. Wu, J. Liu, and O. V. Yazyev, Nano Lett. **23**, 2921 (2023).
[57] F. Wu, T. Lovorn, E. Tutuc, I. Martin, and A. H. MacDonald, Phys. Rev. Lett. **122**, 086402 (2019).
[58] N. Morales-Durán, N. Wei, J. Shi, and A. H. MacDonald, Phys. Rev. Lett. **132**, 096602 (2024).
[59] T. Devakul, V. Crépel, Y. Zhang, and L. Fu, Nat. Commun. **12**, 6730 (2021).
[60] Y. Su, H. Li, C. Zhang, K. Sun, and S.-Z. Lin, Phys. Rev. Res. **4**, L032024 (2022).
[61] A. P. Reddy, F. Alsallom, Y. Zhang, T. Devakul, and L. Fu, Phys. Rev. B **108**, 085117 (2023).
[62] V. Crépel, N. Regnault, and R. Queiroz, Commun. Phys. **7**, 146 (2024).
[63] C. Wang, X.-W. Zhang, X. Liu, Y. He, X. Xu, Y. Ran, T. Cao, and D. Xiao, Phys. Rev. Lett. **132**, 036501 (2024).
[64] C. Xu, J. Li, Y. Xu, Z. Bi, and Y. Zhang, Proc. Natl. Acad. Sci. USA **121**, e2316749121 (2024).
[65] F.-R. Fan, C. Xiao, and W. Yao, Phys. Rev. B **109**, L041403 (2024).
[66] Y.-M. Xie, C.-P. Zhang, J.-X. Hu, K. F. Mak, and K. T. Law, Phys. Rev. Lett. **128**, 026402 (2022).
[67] M. Serlin, C. Tschirhart, H. Polshyn, Y. Zhang, J. Zhu, K. Watanabe, T. Taniguchi, L. Balents, and A. Young, Science **367**, 900 (2019).
[68] T. Li, S. Jiang, B. Shen, Y. Zhang, L. Li, Z. Tao, T. Devakul, K. Watanabe, T. Taniguchi, L. Fu, J. Shan, and K. F. Mak, Nature (London) **600**, 641 (2021).
[69] H. Polshyn, J. Zhu, M. A. Kumar, Y. Zhang, F. Yang, C. L. Tschirhart, M. Serlin, K. Watanabe, T. Taniguchi, A. H. MacDonald *et al.*, Nature (London) **588**, 66 (2020).
[70] G. Chen, A. L. Sharpe, P. Gallagher, I. T. Rosen, E. J. Fox, L. Jiang, B. Lyu, H. Li, K. Watanabe, T. Taniguchi, J. Jung, Z. Shi, D. Goldhaber-Gordon, Y. Zhang, and F. Wang, Nature (London) **572**, 215 (2019).
[71] S. Wu, Z. Zhang, K. Watanabe, T. Taniguchi, and E. Y. Andrei, Nat. Mater. **20**, 488 (2021).
[72] K. P. Nuckolls, M. Oh, D. Wong, B. Lian, K. Watanabe, T. Taniguchi, B. A. Bernevig, and A. Yazdani, Nature (London) **588**, 610 (2020).
[73] A. T. Pierce, Y. Xie, J. M. Park, E. Khalaf, S. H. Lee, Y. Cao, D. E. Parker, P. R. Forrester, S. Chen, K. Watanabe *et al.*, Nat. Phys. **17**, 1210 (2021).
[74] I. Das, X. Lu, J. Herzog-Arbeitman, Z.-D. Song, K. Watanabe, T. Taniguchi, B. A. Bernevig, and D. K. Efetov, Nat. Phys. **17**, 710 (2021).
[75] E. M. Spanton, A. A. Zibrov, H. Zhou, T. Taniguchi, K. Watanabe, M. P. Zaletel, and A. F. Young, Science **360**, 62 (2018).
[76] Y. Xie, A. T. Pierce, J. M. Park, D. E. Parker, E. Khalaf, P. Ledwith, Y. Cao, S. H. Lee, S. Chen, P. R. Forrester, K. Watanabe, T. Taniguchi, A. Vishwanath, P. Jarillo-Herrero, and A. Yacoby, Nature (London) **600**, 439 (2021).
[77] See Supplemental Material at http://link.aps.org/supplemental/10.1103/PhysRevB.110.075109 for (a) details of the continuum model, (b) details of the renormalization group calculations, (c) detailed formalism for the Hartree-Fock calculations, (d) more results from the exact-diagonalization calculations, (e) integer and fractional Chern insulator states in generic multilayer graphene moiré superlattices aligned with hBN, (f) twist angle dependence of the fractional Chern insulator states in pentalayer graphene moiré superlattice, (g) effects of different alignments of hBN substrates, and (h) lat-

tice relaxations and their effects on electronic band structures, which including Refs. [5,6,61,78,82,83,87,93–109].
[78] P. Moon and M. Koshino, Phys. Rev. B **90**, 155406 (2014).
[79] P. Moon and M. Koshino, Phys. Rev. B **87**, 205404 (2013).
[80] Y. Jang, Y. Park, J. Jung, and H. Min, Phys. Rev. B **108**, L041101 (2023).
[81] S. Slizovskiy, A. Garcia-Ruiz, A. I. Berdyugin, N. Xin, T. Taniguchi, K. Watanabe, A. K. Geim, N. D. Drummond, and V. I. Fal'ko, Nano Lett. **21**, 6678 (2021).
[82] O. Vafek and J. Kang, Phys. Rev. Lett. **125**, 257602 (2020).
[83] J. Gonzalez, F. Guinea, and M. A. H. Vozmediano, Nucl. Phys. B **424**, 595 (1994).
[84] V. N. Kotov, B. Uchoa, V. M. Pereira, F. Guinea, and A. H. Castro Neto, Rev. Mod. Phys. **84**, 1067 (2012).
[85] A. H. Castro Neto, F. Guinea, N. M. R. Peres, K. S. Novoselov, and A. K. Geim, Rev. Mod. Phys. **81**, 109 (2009).
[86] R. R. Nair, P. Blake, A. N. Grigorenko, K. S. Novoselov, T. J. Booth, T. Stauber, N. M. Peres, and A. K. Geim, Science **320**, 1308 (2008).
[87] X. Lu, S. Zhang, Y. Wang, X. Gao, K. Yang, Z. Guo, Y. Gao, Y. Ye, Z. Han, and J. Liu, Nat. Commun. **14**, 5550 (2023).
[88] S. M. Girvin, A. H. MacDonald, and P. M. Platzman, Phys. Rev. B **33**, 2481 (1986).
[89] Z. Dong, A. S. Patri, and T. Senthil, arXiv:2311.03445.
[90] B. Zhou, H. Yang, and Y.-H. Zhang, arXiv:2311.04217.
[91] J. Dong, T. Wang, T. Wang, T. Soejima, M. P. Zaletel, A. Vishwanath, and D. E. Parker, arXiv:2311.05568.
[92] J. Herzog-Arbeitman, Y. Wang, J. Liu, P. M. Tam, Z. Qi, Y. Jia, D. K. Efetov, O. Vafek, N. Regnault, H. Weng, Q. Wu, B. A. Bernevig, and J. Yu, Phys. Rev. B **109**, 205122 (2024).
[93] E. McCann, Phys. Rev. B **74**, 161403(R) (2006).
[94] A. A. Avetisyan, B. Partoens, and F. M. Peeters, Phys. Rev. B **79**, 035421 (2009).
[95] A. A. Avetisyan, B. Partoens, and F. M. Peeters, Phys. Rev. B **80**, 195401 (2009).
[96] M. Koshino and E. McCann, Phys. Rev. B **79**, 125443 (2009).
[97] F. Zhang, B. Sahu, H. Min, and A. H. MacDonald, Phys. Rev. B **82**, 035409 (2010).
[98] D. C. Elias, R. Gorbachev, A. Mayorov, S. Morozov, A. Zhukov, P. Blake, L. Ponomarenko, I. Grigorieva, K. Novoselov, F. Guinea *et al.*, Nat. Phys. **7**, 701 (2011).
[99] S. Zhang, X. Lu, and J. Liu, Phys. Rev. Lett. **128**, 247402 (2022).
[100] C. Moulsdale, A. Knothe, and V. Fal'ko, Phys. Rev. B **105**, L201112 (2022).
[101] Z. Wang, Y. B. Wang, J. Yin, E. Tóvári, Y. Yang, L. Lin, M. Holwill, J. Birkbeck, D. J. Perello, S. Xu, J. Zultak, R. V. Gorbachev, A. V. Kretinin, T. Taniguchi, K. Watanabe, S. V. Morozov, M. Andelković, S. P. Milovanović, L. Covaci, F. M. Peeters *et al.*, Sci. Adv. **5**, eaay8897 (2019).
[102] L. Wang, S. Zihlmann, M.-H. Liu, P. Makk, K. Watanabe, T. Taniguchi, A. Baumgartner, and C. Schonenberger, Nano Lett. **19**, 2371 (2019).
[103] A. P. Thompson, H. M. Aktulga, R. Berger, D. S. Bolintineanu, W. M. Brown, P. S. Crozier, P. J. in 't Veld, A. Kohlmeyer, S. G. Moore, T. D. Nguyen, R. Shan, M. J. Stevens, J. Tranchida, C. Trott, and S. J. Plimpton, Comput. Phys. Commun. **271**, 108171 (2022).
[104] N. Leconte, S. Javvaji, J. An, A. Samudrala, and J. Jung, Phys. Rev. B **106**, 115410 (2022).
[105] N. N. T. Nam and M. Koshino, Phys. Rev. B **96**, 075311 (2017).
[106] M. Long, P. A. Pantaleón, Z. Zhan, F. Guinea, J. Á. Silva-Guillén, and S. Yuan, npj Comput. Mater. **8**, 73 (2022).
[107] M. Koshino and N. N. T. Nam, Phys. Rev. B **101**, 195425 (2020).
[108] B. Xie and J. Liu, Phys. Rev. B **108**, 094115 (2023).
[109] S. Zhang, X. Dai, and J. Liu, Phys. Rev. Lett. **128**, 026403 (2022).